*J. Fluid Mech.* (1977), *vol.* 81, *part* 3, *pp.* 565–592
*Printed in Great Britain*



# Cellular convection with liquid-film flow

By E. JAMES DAVIS AND C. K. CHOI
Department of Chemical Engineering, Clarkson College of Technology, Potsdam, New York 13676

(Received 26 January 1976)

This paper is a theoretical and experimental investigation of the onset of the buoyancy-driven longitudinal roll cells that occur when a liquid layer flows over a heated horizontal plate. Linear stability theory is applied under the assumption that the spatially developing temperature profile can be treated locally, that is at each axial position, as being 'frozen'. Using the film thickness as the length scaling factor, the critical Rayleigh numbers associated with the onset of longitudinal rolls are found to be considerably lower than measured values. A modified local stability analysis using the thermal boundary-layer thickness as the scaling factor is shown to agree with experiments. Predicted wavenumbers and the position of the onset of cellular convection are in agreement with wavenumbers measured by flow-visualization techniques. The position of the onset of cellular convection is also obtained from heat-transfer measurements at the heated surface. In the asymptotic limit of a linear undisturbed temperature profile the classical solutions of the Rayleigh–Bénard problem for the critical Rayleigh number and wavenumber are recovered, the only effect of the flow being the structure of the secondary flow that occurs when the system is unstable. Amplification theory is also compared with experimental data for the position at which the thermal effects of the convection are detectable and for the wavenumbers measured by flow visualization. The thermal amplification ratio $\overline{Nu}$ and a velocity-disturbance amplification ratio $\overline{w}$ are used to interpret the onset of discernible cellular convection. The data are not consistent with any single amplification ratio over the range of Rayleigh numbers studied ($10^3 < Ra < 3 \times 10^5$), and the theoretical and experimental results suggest that a band of wavenumbers rather than a single wavenumber is encountered when cellular convection occurs.

## 1. Introduction

When a fluid is heated from below the vertical temperature gradient in the fluid leads to a potentially unstable density gradient. Convective motion, driven by the buoyancy of the hotter fluid near the heated surface, occurs when the density variation become sufficiently large to overcome the stabilizing effects of viscosity and thermal conduction. In the classical problem of heating an initially stagnant liquid layer, the Rayleigh–Bénard problem (RBP, for brevity), convective motion occurs when the Rayleigh number ($Ra^* = \beta g d^3 \Delta T/\alpha\nu$ for constant-temperature boundary conditions and $Ra = \beta g q_w d^4/\alpha k\nu$ for constant heat flux) exceeds a critical value $Ra_c$ that depends on the thermal and hydrodynamic boundary conditions at the upper and lower surfaces. The parameters in the Rayleigh numbers are: $\beta$, the coefficient of volumetric expansion; $g$, the gravitational acceleration; $d$, the liquid layer's thickness; $\Delta T$, the

temperature difference across the layer; $q_w$, the wall heat flux; $\alpha$, the thermal diffusivity; $k$, the thermal conductivity, and $\nu$, the kinematic viscosity.

Since Rayleigh (1916) analysed the onset of thermal convection apparently corresponding to Bénard's (1900) experiments an extensive literature has evolved around the RBP and related problems. Because Chandrasekhar's (1961) treatise covers the principles of hydrodynamic stability and Berg, Acrivos & Boudart (1966) and Whitehead (1971) have reviewed the field of cellular convection, we need mention only the studies most germane to the present work.

It should be pointed out that even with the classical RBP there are numerous complications that can arise. It is well established that surface-tension variations can also produce cellular convection (Marangoni instability), and some of Bénard's observations were of surface-tension-driven instabilities. Another complication emerges when the rate of heating is high, for in this event the undisturbed temperature field is nonlinear and time dependent, and the question of the time required to reach the onset of convective motion arises.

Soberman (1959) and Nielsen & Sabersky (1973) reported experimental results showing that rapid heating apparently increases the Rayleigh number required to initiate thermal convection, and Morton (1957) analysed the problem of time-dependent heating for the special case wherein the deviations from a linear density gradient are small by using conventional marginal-stability concepts. Lick (1965) and Currie (1967) applied a quasi-steady approach in which the transient and nonlinear undisturbed temperature profile was approximated by two linear segments. Foster (1965), Mahler, Schechter & Wissler (1968) and Gresho & Sani (1971) questioned quasi-steady analysis, claiming that the quasi-steady model is a poor one owing to the effect of the rapid variation of the undisturbed temperature profile on the onset of instabilities. Contrary to the concept of the marginal state, they suggested redefining the critical Rayleigh number as occurring when the motion is first discernible. Assuming some initial disturbance, typically 'white noise', Foster, Mahler *et al.* and Gresho & Sani considered the critical state to be attained at the time when the fastest-growing disturbance has grown sufficiently to be observed, i.e. when the initial disturbance has been amplified by several orders of magnitude. But this definition lacks uniqueness since it involves the measurability of discernible motion, which in turn involves the measurement technique.

As we shall show, the time-dependent RBP is closely related mathematically and conceptually to the present problem, which involves spatial growth of disturbances, but the convective motion that ensues above the critical Rayleigh number is quite different when the liquid layer is flowing.

Although we shall examine the problem of convective instability brought about by an adverse temperature gradient, the problem of convective motion also arises when concentration gradients produce unstable density gradients.

Plevan & Quinn (1966) and Blair & Quinn (1969) studied experimentally the convective motion associated with unstable density gradients produced by unsteady-state gas absorption in an initially quiescent liquid layer, and the latter compared their results with Foster's (1968) amplification theory. The results are inconclusive since amplification ratios of from $10^3$ to $10^8$ were required for consistency with the data on the onset of cellular convection. Their amplification ratio $\bar{w}$ is defined by

$$\bar{w}(t) = [\langle w^2(t,z)\rangle / \langle w^2(0,z)\rangle]^{\frac{1}{2}},$$

where $w$ is the vertical component of the non-dimensional velocity perturbation and $w(0, z)$ is the assumed initial disturbance. The angular brackets indicate integration over the film thickness, i.e.

$$\langle w^2(t, z)\rangle = \int_0^1 w^2(t, z)\, dz.$$

If amplification ratios as large as $10^8$ must be invoked to obtain agreement between theory and experiment, few conclusions can be drawn because linear stability theory is not likely to be valid when such a large amplification of disturbances has occurred.

Lower amplification ratios were consistent with the experimental results of Davenport & King (1974*a*, *b*), who studied the onset of natural convection in deep pools heated from below and at gas–liquid interfaces by cooling the upper surface of an air gap above a liquid pool. The onset of convection for a gas–liquid system was found to be very similar to that for a liquid–solid surface. On comparing their data on the $Ra$ at which convection was first observed with Foster's amplification theory, they found their results to be consistent with $\overline{w} = 10^1$ or $10^2$ at high Prandtl numbers ($Pr = \nu/\alpha > 100$) and with $\overline{w} = 10^2$ or $10^4$ for $Pr = 10$.

A study closely related to the present work is that of Tobias & Hickman (1965), who measured the effects of buoyancy forces on ionic mass transfer at horizontal planar electrodes with laminar and turbulent flow between the parallel plates. They successfully correlated data for free-convection control and for stable laminar convective diffusion. They postulated the existence of roll cells as the secondary flow that occurs at higher Rayleigh numbers, and electrode deposits on their cathode provided evidence in the form of streaks that roll cells had occurred.

Hung & Davis (1974*a*, *b*) observed and measured the onset of similar roll cells in their study of heat transfer to the liquid layer of a horizontal stratified gas–liquid flow, and they showed that with combined free and forced convection the Nusselt number can be increased by more than 300 % over the Nusselt number for pure forced convection. The boundaries of the roll cells were observed by flow visualization with a water-soluble dye, and the axial position of the onset of free convection was determined by flow visualization and heat-transfer measurements. Hung & Davis (1974*a*) analysed this space-dependent analogue of the time-dependent RBP by means of linear stability analysis using the quasi-static (or 'frozen' temperature profile) assumption of Morton (1957), Lick (1965) and Currie (1967). The predicted critical Rayleigh numbers were found to be significantly lower than experimental values.

It is the purpose of the present work to extend both the theoretical analysis and the experimental work of Hung & Davis to elucidate the mechanism of roll-cell formation, to test the assumption of the quasi-static (or quasi-steady) temperature profile, and to predict the onset of cellular convection for liquid-film flow. In addition, we analyse the stability problem by means of amplification theory, comparing the results of analysis with our experiments.

## 2. The unperturbed system

Consider the system examined by Hung & Davis (1974*a*) and shown in figure 1. The only effect of the concurrent gas flow here is to produce motion of the liquid film, and when the axial pressure gradient is sufficiently small, which is true of the

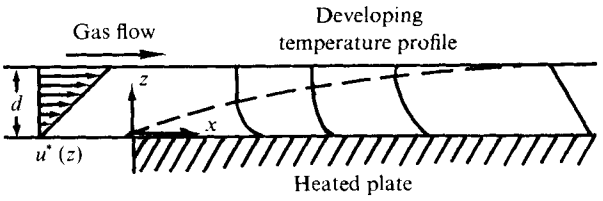


FIGURE 1. The system under consideration.

experiments to be considered, the liquid flow closely approximates Couette flow. There is no additional complication if the analysis is extended to Poiseuille flow between parallel plates, which is the system studied by Tobias & Hickman, but the details of the computations are somewhat different as we shall indicate.

It should be pointed out that concurrent gas–liquid flows are potentially unstable with respect to long interfacial waves and short Tollmien–Schlichting waves as recently discussed by Gumerman & Homsy (1974*a*, *b*), but these instabilities do not occur under most of the conditions of interest here. At the higher gas and liquid flow rates of the experiments, however, interfacial waves were suppressed by using trace amounts of a soluble surfactant.

For a sufficiently large aspect ratio (plate width to liquid-film thickness) the edge effects can be neglected and the non-dimensional unperturbed velocity and temperature distributions are given by

$$U(\zeta) = 2\zeta \tag{1}$$

and

$$\Theta(\xi, \zeta) = 1 - \zeta - \sum_{n=1}^{\infty} K_n \exp(-\tfrac{1}{2}\lambda_n^2 \xi)\, \psi_n(\zeta), \tag{2}$$

where the eigenfunctions $\psi_n(\zeta)$ are given by

$$\psi_n(\zeta) = \zeta^{\frac{1}{2}} J_{-\frac{1}{3}}(\tfrac{2}{3}\lambda_n \zeta^{\frac{3}{2}}). \tag{3}$$

The coefficients $K_n$ are constructed to produce a uniform inlet temperature, i.e. $\Theta(0, \zeta) = 0$, and are given by

$$K_n = 3^{\frac{4}{3}}/\Gamma(\tfrac{2}{3})\, \lambda_n^{\frac{7}{3}} J_{\frac{2}{3}}^2(\tfrac{2}{3}\lambda_n), \tag{4}$$

where $\Gamma(x)$ represents the gamma function and $J_\nu(x)$ is the Bessel function of order $\nu$. The non-dimensional co-ordinates are defined as $\xi = x/dPe$, $\eta = y/d$ and $\zeta = z/d$, where the Péclet number is $Pe = d\bar{u}/\alpha$. The liquid-film thickness is $d$, $\bar{u}$ is the average velocity of the liquid film and $\alpha$ is the thermal diffusivity of the liquid. The non-dimensional velocity and temperature variables are defined by $U = u^*/\bar{u}$, $V = v^*d/\alpha$, $W = w^*d/\alpha$ and $\Theta = (T - T_0)/(q_w d/k)$, where $(u^*, v^*, w^*)$ is the dimensional velocity vector, $T$ is the dimensional temperature, $T_0$ is the inlet temperature (which is also the interfacial temperature here), $q_w$ is the heat flux at the heated surface and $k$ is the thermal conductivity of the liquid.

Note that we are considering constant wall heat flux and uniform free-surface temperature boundary conditions. For these conditions the eigenvalues $\lambda_n$ are obtained as the zeros of the following transcendental equation:

$$J_{-\frac{1}{3}}(\tfrac{2}{3}\lambda_n) = 0, \tag{5}$$

which gives $\lambda_1 = 2{\cdot}79952$, $\lambda_2 = 7{\cdot}48177$, $\lambda_3 = 12{\cdot}1863, \ldots$. The higher eigenvalues have been tabulated by Choi (1976).

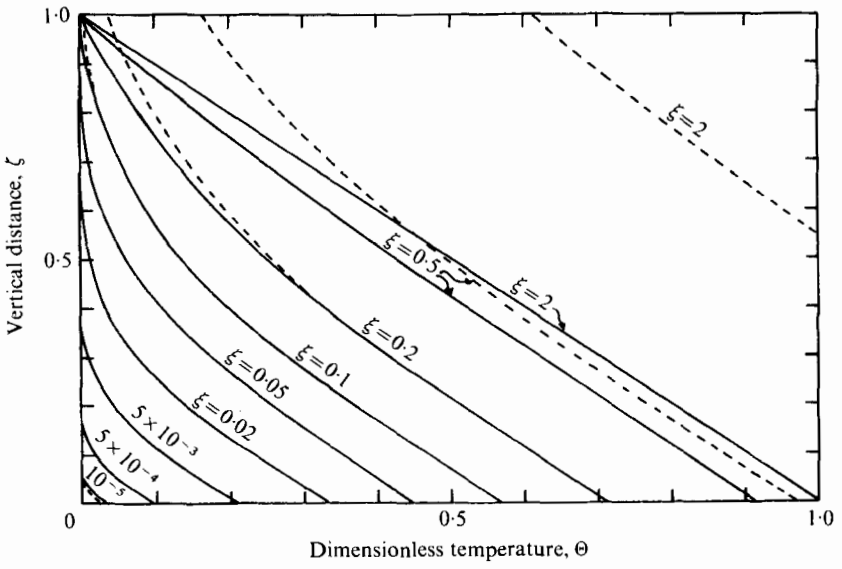


FIGURE 2. The unperturbed temperature distributions. Solution: ——, Graetz; – – –, Leveque.

For Poiseuille flow between parallel plates the undisturbed temperature field is obtained in terms of confluent hypergeometric functions as shown by Davis (1973), but the general structure of the problem solution is the same, and any appropriate linear boundary conditions can be treated.

The eigenfunction solution (Graetz solution) given by (2) is computationally inconvenient for small values of $\xi$ because of the slow convergence of the series expansion, so for small $\xi$ we have used the Leveque solution

$$\Theta(\omega) = \frac{(\frac{9}{2}\xi)^{\frac{1}{3}}}{\Gamma(\frac{2}{3})}[e^{-\omega^3} - \omega\Gamma(\tfrac{2}{3}, \omega^3)], \tag{6}$$

where $\omega = \zeta/(\frac{9}{2}\xi)^{\frac{1}{3}}$ and $\Gamma(a, b)$ is the incomplete gamma function.

The temperature distributions predicted by (2) and (6) are shown in figure 2. The asymptotic limit of a linear temperature profile is seen to occur for $\xi > 1$, and the region $0 \leqslant \xi < 1$ corresponds to the thermal entry region. The temperature distribution in the thermal entry region is similar to the unsteady-state temperature distribution in a stagnant liquid layer, but under the steady-state conditions of the present problem an instability that develops does so spatially. Deviations from the undisturbed temperature distribution caused by natural convection are best determined experimentally by measuring the axially varying Nusselt number defined by $Nu = hd/k$, where the heat-transfer coefficient $h$ is calculated from the definition $h = q_w/(T_m - T_w)$, in which $q_w$ is the local wall heat flux, $T_m$ is the mixing-cup temperature of the liquid film and $T_w$ is the local wall temperature.

From the definitions of the Nusselt number and the mixing-cup temperature, the Nusselt number $Nu_f$ for pure forced convection, becomes

$$Nu_f = \left\{\frac{2}{3} - \sum_{n=1}^{\infty} \frac{K_n}{\lambda_n^{\frac{1}{3}}}\left[\frac{3^{\frac{1}{3}}}{\Gamma(\frac{2}{3})} - \frac{2}{\lambda_n^{\frac{1}{3}}} J_{\frac{1}{3}}(\tfrac{2}{3}\lambda_n)\right] \exp\left(-\frac{\lambda_n^2 \xi}{2}\right)\right\}^{-1} \tag{7}$$

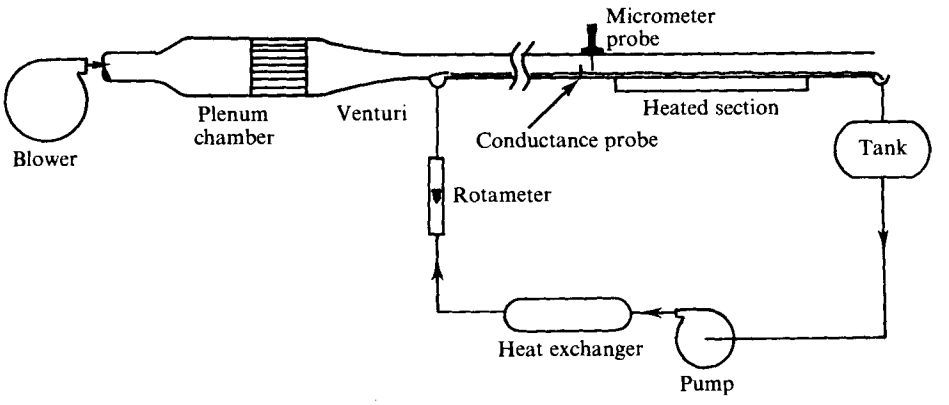


FIGURE 3. Schematic diagram of the experimental equipment.

if the temperature distribution (2) is used and

$$Nu_f = \Gamma(\tfrac{2}{3})\left\{(\tfrac{9}{2}\xi)^{\frac{1}{3}} - 3\xi\left[\tfrac{1}{3}\Gamma(\tfrac{2}{3}) + \left(\frac{2}{9\xi}\right)^{\frac{2}{3}}\exp\left(-\frac{2}{9\xi}\right) - \left(\frac{1}{3}+\frac{2}{9\xi}\right)\Gamma\left(\frac{2}{3}, \frac{2}{9\xi}\right)\right]\right\}^{-1} \quad (8)$$

if (6) is used.

Before proceeding to the analysis of the perturbed system it is instructive to examine the results of experiments to establish the heat-transfer characteristics of the combined free and forced convection.

## 3. Heat-transfer experiments

The experimental facility used to obtain heat-transfer data was essentially that used by Hung & Davis (1974*b*) and described by Frisk & Davis (1972). Briefly, a water–wind tunnel, shown schematically in figure 3, was equipped for measuring the relevant fluid-mechanical and heat-transfer parameters. The apparatus consisted of a turbocompressor for supplying the air flow, a spray chamber in which the air was saturated to prevent evaporation of the liquid phase, a rectangular Plexiglas duct (2·5 cm high and 25 cm wide), a heat-transfer section consisting of an electrically heated copper block installed flush with the tunnel bottom and a recycling system for the liquid phase. Thermocouples inserted in the copper block were used to measure the wall temperature profile, and the liquid-film thickness was measured by means of a micrometer probe and an electrical conductance probe. Interfacial velocities were measured by placing small particles on the liquid surface and recording the time required for them to move between two axial positions. The heat flux was measured and controlled by means of six banks of powerstats each of which supplied heat to a section of the copper block. To minimize axial conduction in the block the six sections were separated by 1 mm Teflon sheets. More complete information about the experimental equipment and procedure is given by Choi (1976).

By varying the gas and liquid flow rates and the power to the heating elements a wide range of Rayleigh numbers could be studied. Local Nusselt numbers were calculated from the heat flux, wall temperature and mixing-cup temperatures (obtained by energy balance). Typical results are shown in figure 4 as Nusselt number *vs.* non-dimensional axial distance for various Rayleigh numbers. Because the mixing-cup

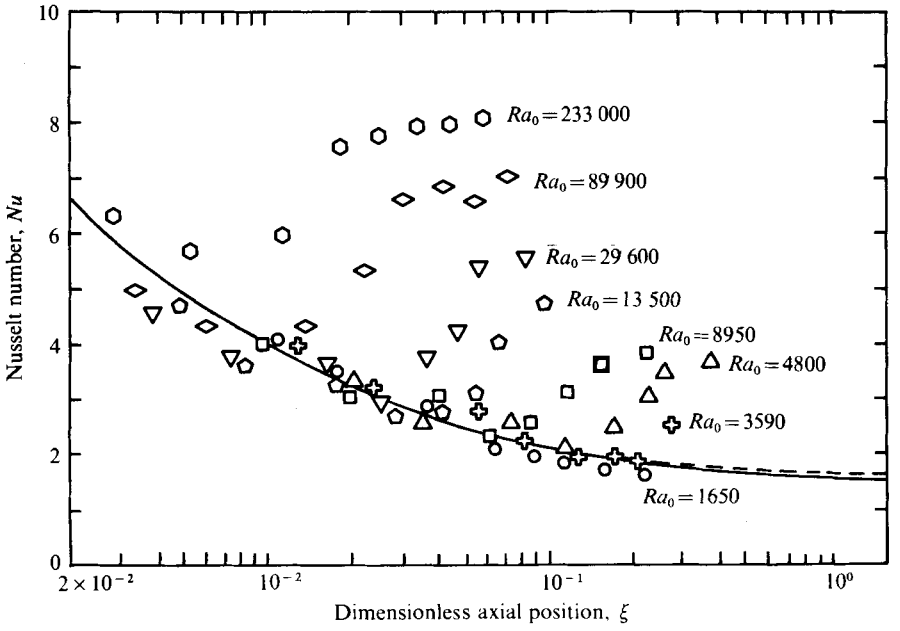


FIGURE 4. Experimental Nusselt numbers as a function of axial position for various Rayleigh numbers. The solid and dashed curves are the results predicted by (7) and (8) for pure forced convection.

temperature and the physical properties varied in the axial direction the Rayleigh number varied, and the Rayleigh numbers indicated on the figure are based on the physical properties and temperatures at the leading edge of the heat-transfer test section.

Figure 4 shows that, within the limits of experimental error, the experimental Nusselt numbers agree with (7) and (8) near the leading edge of the heated section. At some axial distance that depends on the Rayleigh number, the Nusselt numbers increasingly deviate from the prediction for pure forced convection. When the heated plate is sufficiently long it is observed that the Nusselt number attains an asymptotic value larger than that for pure forced convection, and the asymptotic value increases with increased Rayleigh number. Although heat-transfer measurements show the effect of the instability, the mode of the instability has been examined by means of flow visualization.

## 4. Flow-visualization experiments

Preliminary studies using a potassium permanganate solution (see Hung & Davis 1974*b*) showed evidence of roll cells initiating at the axial positions corresponding to the minima in the Nusselt numbers discussed above. Better results have been obtained using a commercially available tracer: Rheoscopic Fluid AQ 1000 (Kalliroscope Co., Cambridge, Massachusetts). A 0·6 % aqueous solution of the tracer was added to the water feed, and photographs were taken at the heat-transfer test section from which the dimensions of the roll cells could be obtained. Figure 5 (plate 1) shows an overall view of the heat-transfer plate after the system had been operated for about six hours to permit deposition of some of the colloidal particles on the bottom of the tunnel.

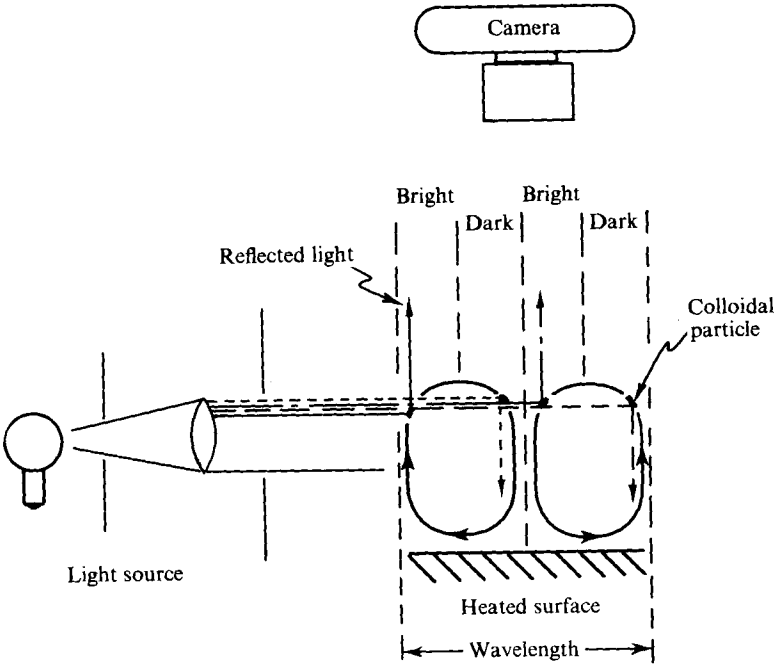


FIGURE 6. Schematic diagram of the photographic set-up used to measure the wavelengths of the roll cells.

Deposition occurred uniformly in the upstream region of the heated plate and along the lines marking the downward flow in the roll cells. The boundaries of the roll cells are clearly evident in the photograph, but the onset of convection is not sharply defined because of the exceptionally long operation of the system. During the six hours of deposition, voltage fluctuations and flow variations were sufficient to cause non-uniform deposition in the flow direction.

To measure the roll-cell dimensions photographs were taken from directly above the heated plate with a light beam from a strobelight directed perpendicular to the axis of the camera. Figure 6 is a schematic diagram of the photographic arrangement. A light beam passing normal to the roll cells was reflected off colloidal particles that were aligned with the streamlines of the flow. The result, seen from above, is a series of light and dark bands, each pair of which corresponds to a single roll cell. If the light source is moved to the right-hand side of figure 6, the light and dark bands reverse as shown by Choi (1976) in a thesis. By counting the number of pairs of such bands over a given width of test section the average wavelength of the roll cells may readily be determined from photographs. The wavenumber is given by

$$a = 2\pi d/\Lambda,$$

where $\Lambda$ is the measured wavelength and $d$ is the film thickness. Figure 6 (plate 2) shows typical roll cells at two different axial positions along the heated surface. At the lower Rayleigh number ($Ra = 2{\cdot}2 \times 10^5$) a cellular secondary flow occurs, but for $Ra = 2{\cdot}7 \times 10^5$ transverse perturbations appear to produce a second instability leading to a turbulent film.

## 5. The perturbation equations

We have analysed the onset of the cellular motion described above by means of linear stability theory. As the formulation of the governing equations is conventional, we shall merely sketch the assumptions and list the resulting equations. It is clear from the nature of the problem that the growth of disturbances is spatially dependent and time independent, so we can eliminate time derivatives. Since the Péclet number ($Pe = d\bar{u}/\alpha$) is large here we can neglect axial conduction. Applying the Boussinesq approximation for the density and denoting unperturbed quantities by a capital letter and perturbations by a lower case letter, the linearized governing equations become

$$\nabla . \mathbf{u} = 0 \quad \text{(continuity)}, \tag{9}$$

$$\frac{1}{Pr}\left(U\frac{\partial \mathbf{u}}{\partial \xi} + w\frac{\partial \mathbf{U}}{\partial \zeta}\right) = -\nabla_2 p + \nabla_2^2 \mathbf{u} + Ra\,\theta \mathbf{k} \quad \text{(equation of motion)}, \tag{10}$$

$$U\frac{\partial \theta}{\partial \xi} + \left(u\frac{\partial}{\partial \xi} + w\frac{\partial}{\partial \zeta}\right)\Theta = \nabla_2^2 \theta \quad \text{(energy equation)}, \tag{11}$$

where $U$ is given by (1), $\nabla_2$ is the two-dimensional operator $\mathbf{j}\,\partial/\partial\eta + \mathbf{k}\,\partial/\partial\zeta$ and the perturbation velocity vector is $\mathbf{u} = \mathbf{i}u + \mathbf{j}v + \mathbf{k}w$, where $u$, $v$ and $w$ are the non-dimensional velocity perturbations in the $x$, $y$ and $z$ directions respectively. The Prandtl and Rayleigh numbers are $Pr = \nu/\alpha$ and $Ra = \beta g q_w d^4/\alpha k \nu$ respectively, and the non-dimensional pressure perturbation is given by $p = p^* d^2/\mu\alpha$, where $p^*$ is the dimensional pressure.

The boundary conditions are

$$u = v = w = \partial\theta/\partial\zeta = 0 \quad \text{at} \quad \zeta = 0. \tag{12}$$

At the upper (free) boundary we assume that there are no perturbations in the tangential stresses and no surface deformation. Also, considering the gas–liquid interface to be isothermal owing to heat transfer to the isothermal turbulent gas phase, the interfacial boundary conditions become

$$\partial u/\partial\zeta = \partial v/\partial\zeta = w = \theta = 0 \quad \text{at} \quad \zeta = 1. \tag{13}$$

The remaining boundary conditions are generated from the equation of continuity using conditions (12) and (13):

$$\partial w/\partial\zeta = 0 \quad \text{at} \quad \zeta = 0, \tag{14}$$

$$\partial^2 w/\partial\zeta^2 = 0 \quad \text{at} \quad \zeta = 1. \tag{15}$$

We shall make one additional simplification based on the results of Hung & Davis (1974*a*): we shall examine the limiting case of large Prandtl number ($Pr \to \infty$). Hung & Davis showed that the effect of lowering the Prandtl number is to lower the predicted critical Rayleigh number for the onset of free convection.

Up to this point our analysis parallels that of Hung & Davis, but our solution procedure differs. Although our results will be identical to those of Hung & Davis when we treat the problem as formulated above, the new method of solution provides the basis for improving the analysis by rescaling to incorporate the thermal boundary-layer thickness.

For large $Pr$, (10) simplifies to

$$\nabla_2^2 \mathbf{u} + Ra\,\theta \mathbf{k} = \nabla_2 p. \tag{16}$$

Since $u$ vanishes at the boundaries and $\partial u/\partial\zeta$ is assumed to vanish at the free surface, only the trivial solution, $u = 0$, satisfies the system of equations. That is, for large $Pr$ and large $Pe$ thermal disturbances do not affect the axial velocity. This result is not inconsistent with our expectations that the most preferred mode of disturbance marking the onset of thermal convection will be a regular longitudinal roll with the secondary flow described by perturbation velocity components $v$ and $w$.

Because of the very large aspect ratio associated with the liquid layer (25 cm wide by $\sim$ 5 mm thick) in this study we can look for a solution in terms of the transverse wavenumber $a$ as follows. Assume that the disturbances have the form

$$(v, w, \theta, p) = (\hat{v}, \hat{w}, \hat{\theta}, \hat{p})\, e^{ia\eta}. \tag{17}$$

Using these relationships and eliminating $\hat{p}$ and $\hat{v}$ from the governing equations, we obtain

$$(D^2 - a^2)^2 \hat{w} - Ra\, a^2 \hat{\theta} = 0 \tag{18}$$

and

$$[2\zeta\, \partial/\partial\xi - (D^2 - a^2)]\hat{\theta} + \hat{w} D\Theta = 0 \tag{19}$$

with the boundary conditions

$$\hat{w}(\xi, 0) = \hat{w}(\xi, 1) = D\hat{w}(\xi, 0) = D^2\hat{w}(\xi, 1) = 0 \tag{20}$$

and

$$\hat{\theta}(\xi, 1) = D\hat{\theta}(\xi, 0) = 0, \tag{21}$$

where $D = \partial/\partial\zeta$.

The essential differences between this set of equations and the classical Rayleigh–Bénard problem are the fact that the undisturbed temperature $\Theta$ is a function of both $\xi$ and $\zeta$ and the presence of the axial convection term $2\zeta\, \partial\hat{\theta}/\partial\xi$ in (19). Both of these additions complicate the problem somewhat. This problem is closely related to the unsteady-state RBP as is made clear by examination of (19). If the velocity distribution were taken to be uniform (slug flow) the convective term in the equation would become $U_0 \partial\hat{\theta}/\partial\xi$, where $U_0$ is the constant uniform velocity. In this case, by setting $\tau = \xi/U_0$ we obtain the unsteady-state heating problem of Foster and Gresho & Sani. The undisturbed temperature distribution $\Theta$ in this case would also reduce to theirs. Thus we can anticipate that the essential features of the unsteady-state Rayleigh–Bénard stability problem will carry over to our spatially dependent problem.

We shall examine the stability characteristics of (18)–(21) from two points of view in this paper. First we shall consider the stability under the assumption that at each axial plane $\xi = \xi_1, \xi_2, \ldots$, we can consider the instability as arising owing to the local temperature distribution without considering the axial rate of change of temperature. This approximation is equivalent to the quasi-static assumption used by Morton (1957), Lick (1965) and Currie (1967) for the unsteady-state RBP and is subject to the criticism raised by Foster (1965) and Gresho & Sani (1971). In a subsequent section we re-examine the problem, relaxing this assumption.

## 6. The Galerkin solution

The problem as stated above involves the question of how the temperature field evolves from that of a developing thermal boundary layer that is axially dependent to a stable secondary flow (roll cells) that is largely independent of axial position (except for the fact that with a constant-heat-flux system $Ra$ changes somewhat in

the axial direction). We cannot simply look for disturbances proportional to $e^{\sigma\xi}$, so we shall use a Galerkin scheme to approximate the solution.

The trial functions are chosen to be the space-dependent Fourier series

$$\hat{w}(\xi,\zeta) = \sum_{i=1}^{\infty} A_i(\xi)\, B_i(\zeta), \tag{22}$$

where
$$B_i(\zeta) = \frac{\sinh\gamma_i(1-\zeta)}{\sinh\gamma_i} - \frac{\sin\gamma_i(1-\zeta)}{\sin\gamma_i} \tag{23}$$

and the eigenvalues $\gamma_i$ satisfy

$$\coth\gamma_i - \cot\gamma_i = 0, \tag{24}$$

which gives $\gamma_1 = 3{\cdot}92660$, $\gamma_2 = 7{\cdot}06858$, $\gamma_3 = 10{\cdot}2101, \ldots$. Similarly

$$\hat{\theta}(\xi,\zeta) = \sum_{j=1}^{\infty} C_j(\xi)\, D_j(\zeta), \tag{25}$$

where
$$D_j(\zeta) = \cos\beta_j\zeta, \quad \beta_j = (j-\tfrac{1}{2})\pi. \tag{26}$$

These expressions have been chosen for the orthogonality properties of the eigenfunctions, and they satisfy the boundary conditions. Substituting these trial functions in (18) and (19) we obtain

$$\sum_{i=1}^{\infty} A_i(\xi)\,[(\gamma_i^4 + a^4)\, B_i(\zeta) - 2a^2 B_i''(\zeta)] - a^2 Ra \sum_{j=1}^{\infty} C_j(\xi)\, D_j(\zeta) = 0 \tag{27}$$

and

$$\sum_{j=1}^{\infty}\left[2\zeta D_j(\zeta)\frac{d}{d\xi}C_j(\xi) + (\beta_j^2 + a^2)\, D_j(\zeta)\, C_j(\xi)\right] + -\sum_{i=1}^{\infty} A_i(\xi)\, B_i(\zeta)\left[1 + \sum_{n=1}^{\infty} K_n\, \Psi_n'(\zeta)\exp\left(-\frac{\lambda_n^2}{2}\xi\right)\right] = 0, \tag{28}$$

where a prime indicates differentiation with respect to $\zeta$.

Multiplying (27) by $B_i(\zeta)$ and (28) by $D_j(\zeta)$ and integrating over $\zeta$ from 0 to 1, we obtain an infinite set of first-order differential equations in $\xi$. By truncating each series after a finite number of terms, the resulting equations can be written in the matrix form

$$(\mathbf{H} - \mathbf{L})\,\mathbf{A}(\xi) - Ra\,\mathbf{M}\mathbf{C}(\xi) = 0 \tag{29}$$

and
$$\mathbf{P}\, d\mathbf{C}(\xi)/d\xi - \mathbf{Q}\mathbf{C}(\xi) - \mathbf{R}(\xi)\,\mathbf{A}(\xi) = 0, \tag{30}$$

where the matrices $\mathbf{H}$, $\mathbf{L}$, $\mathbf{M}$, $\mathbf{P}$, $\mathbf{Q}$ and $\mathbf{R}$ have the following elements:

$$H_{ij} = \frac{\gamma_j^4 + a^4}{2a^2}\delta_{ij}, \quad Q_{ij} = -\frac{\beta_j^2 + a^2}{2}\delta_{ij},$$

$$L_{ij} = \langle B_j \,|\, B_i''\rangle = \begin{cases} \dfrac{4\gamma_i^2\gamma_j^2}{\gamma_i^4 - \gamma_j^4}\left(\dfrac{\gamma_i}{\tanh\gamma_i} - \dfrac{\gamma_j}{\tanh\gamma_j}\right) & \text{for} \quad i \neq j, \\ \dfrac{\gamma_j}{\tanh^2\gamma_j}(\tanh\gamma_j - \gamma_j) & \text{for} \quad i = j, \end{cases}$$

$$M_{ij} = \frac{\langle B_j \,|\, D_i\rangle}{2} = \frac{\gamma_j^3}{(\gamma_j^4 - \beta_i^4)\tanh\gamma_j},$$

$$P_{ij} = 2\langle D_j \,|\, \zeta \,|\, D_i\rangle = \begin{cases} \dfrac{2}{(\beta_i^2 - \beta_j^2)^2}[(-1)^{i+j}\beta_i\beta_j - \tfrac{1}{2}(\beta_i^2 + \beta_j^2)] & \text{for} \quad i \neq j, \\ \tfrac{1}{2}(1 - 1/\beta_j^2) & \text{for} \quad i = j, \end{cases}$$

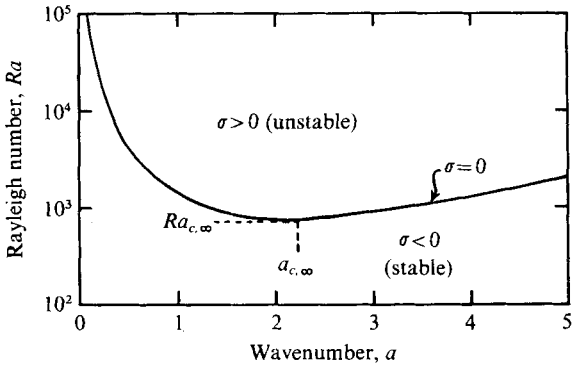


FIGURE 8. The neutral-stability curve for the asymptotic limit of a linear undisturbed temperature profile.

and $$R_{ij}(\xi) = 2M_{ji} - \sum_{k=1}^{K} K_n \lambda_n \exp(-\tfrac{1}{2}\lambda_n^2 \xi) \langle D_j | B_i | \zeta J_{\frac{2}{3}}(\tfrac{2}{3}\lambda_n \zeta^{\frac{3}{2}}) \rangle.$$

Here the operation $\langle f \mid g \rangle$ is defined by

$$\langle f \mid g \rangle = \int_0^1 f(\zeta) g(\zeta) d\zeta.$$

The matrices **H**, **L**, **M**, **P**, **Q** and **R** are $N \times N$ square matrices, where $\mathbf{A}(\xi)$ and $\mathbf{C}(\xi)$ are column vectors with $N$ elements. These matrix equations can be combined to give

$$d\mathbf{C}(\xi)/d\xi = \mathbf{P}^{-1}[\mathbf{Q} + Ra\,\mathbf{R}(\xi)(\mathbf{H} - \mathbf{L})^{-1}\mathbf{M}]\,\mathbf{C}(\xi). \tag{31}$$

The stability characteristics of (31) must be determined to obtain the critical Rayleigh number $Ra_c$ and the wavenumber $a_c$ corresponding to $Ra_c$. To illustrate the solution procedure it is useful to consider first the asymptotic limit $\zeta \to \infty$, which corresponds to a linear unperturbed temperature distribution.

## 7. The asymptotic limit of large $\xi$

For large $\xi$ the elements of $\mathbf{R}(\xi)$ reduce to

$$R_{ij}(\xi) = 2M_{ji} = 2M_{ij}^{\mathrm{T}},$$

where $\mathbf{M}^{\mathrm{T}}$ is the transpose of **M**. Furthermore, $\hat{\theta}$ becomes independent of $\xi$, so $C_j(\xi)$ can be replaced by a constant and thus $d\mathbf{C}/d\xi = 0$. In this case (31) reduces to

$$|\mathbf{Q} + 2Ra\,\mathbf{M}^{\mathrm{T}}(\mathbf{H} - \mathbf{L})^{-1}\mathbf{M}| = 0. \tag{32}$$

Equation (32) has been applied to obtain the neutral-stability curve on a plot of $Ra$ *vs.* $a$, assuming the validity of the principle of exchange of stabilities. The results are shown in figure 8. The minimum in the neutral-stability curve for this asymptotic limit has been calculated to be

$$Ra_{c,\infty} = 816{\cdot}748 \quad \text{at} \quad a_{c,\infty} = 2{\cdot}21.$$

This result is identical to the critical stability criterion for the RBP for constant heat flux at the fixed boundary and constant temperature at the free surface. Thus the flow has no effect on the onset of the instability in the asymptotic region. Furthermore,

the agreement between the critical Rayleigh number calculated here and the result reported by Sparrow, Goldstein & Jonsson (1964) ($Ra_c = 816{\cdot}748$ and $a_c = 2{\cdot}21$) is a test of the accuracy of the Galerkin procedure applied in this study.

To acquire insight into the nature of the instability in the limiting case for $Ra > Ra_{c,\infty}$ we have examined the spatial growth of disturbances. The unperturbed condition of a linear temperature profile which is independent of $\xi$ makes it possible to look for a solution of the form

$$[\hat{w}(\xi,\zeta), \hat{\theta}(\xi,\zeta)] = [w^*(\zeta), \theta^*(\zeta)]\, e^{\sigma\xi}, \tag{33}$$

where $\sigma$ is the spatial growth constant. Using this form of the solution and setting $D\Theta = -1$ (the asymptotic temperature gradient) in (19), (18) and (19) can be combined to give

$$\{[2\sigma\zeta - (D^2-a^2)]\,(D^2-a^2)^2 - a^2\,Ra\}\, w^* = 0 \tag{34}$$

with boundary conditions

$$w^*(0) = Dw^*(0) = w^*(1) = D^2w^*(1) = 0 \tag{35}$$

and

$$(D^2-a^2)^2\, w^*(1) = D(D^2-a^2)^2\, w^*(0) = 0. \tag{36}$$

This system of equations can be solved by applying the method of Sparrow *et al.* (1964), which uses a rapidly converging power series to obtain the maximum growth rate $\sigma_c$ and the corresponding wavenumber $a_c$ for $Ra > Ra_{c,\infty}$.

Let

$$w^*(\zeta) = \sum_{k=0}^{5} H_k f^{(k)}(\zeta) \tag{37}$$

and

$$f^{(k)}(\zeta) = \sum_{l=0}^{\infty} b_l^{(k)}\, \zeta^l, \tag{38}$$

where $b_{-1}^{(k)} = 0$, $b_l^{(k)} = \delta_{lk}$ for $0 \leqslant l \leqslant 5$ and

$$b_l^{(k)} = (l!)^{-1}\{3a^2(l-2)!\, b_{l-2}^{(k)} + 2\sigma(l-6)\,(l-3)!\, b_{l-3}^{(k)} - 3a^4(l-4)!\, b_{l-4}^{(k)} - 4\sigma a^2(l-6)\,(l-5)!\, b_{l-5}^{(k)} + a^2(l-6)!\,[(a^4-Ra)\, b_{l-6}^{(k)} + 2\sigma a^2 b_{l-7}^{(k)}]\} \quad \text{for} \quad l \geqslant 6.$$

The coefficients $H_k$ are chosen to satisfy the boundary conditions. From the boundary conditions at $\zeta = 0$ we obtain $H_0 = H_1 = 0$ and $H_5 = \frac{1}{10}a^2H_3$, and the conditions at $\zeta = 1$ generate the following secular equation:

$$\begin{vmatrix} f^{(2)} & f^{(3)} + \frac{1}{10}a^2 f^{(5)} & f^{(4)} \\ f^{(2)''} & f^{(3)''} + \frac{1}{10}a^2 f^{(5)''} & f^{(4)''} \\ f^{(2)\mathrm{iv}} & f^{(3)\mathrm{iv}} + \frac{1}{10}a^2 f^{(5)\mathrm{iv}} & f^{(4)\mathrm{iv}} \end{vmatrix} = 0, \tag{39}$$

where the primes denote differentiation with respect to $\zeta$. For a particular $\sigma_c$ the minimum $Ra$ that satisfies (39) is obtained by means of a plot of $Ra$ *vs.* $a$. In this way we calculated the results shown in figure 9, which shows that the maximum growth rate and the critical wavenumber increase almost linearly with $Ra$ for $Ra > Ra_{c,\infty}$. The critical values $Ra_{c,\infty}$ and $a_{c,\infty}$ for $\sigma = 0$ obtained in this way are identical to those calculated from the Galerkin scheme.

We conclude from these asymptotic results that for $Ra > Ra_{c,\infty}$ disturbances grow exponentially in space, which is the usual result of linear stability theory. Of course, after some sufficiently large distance the disturbances will be too large to permit the neglect of nonlinear terms, and the analysis will be invalid.

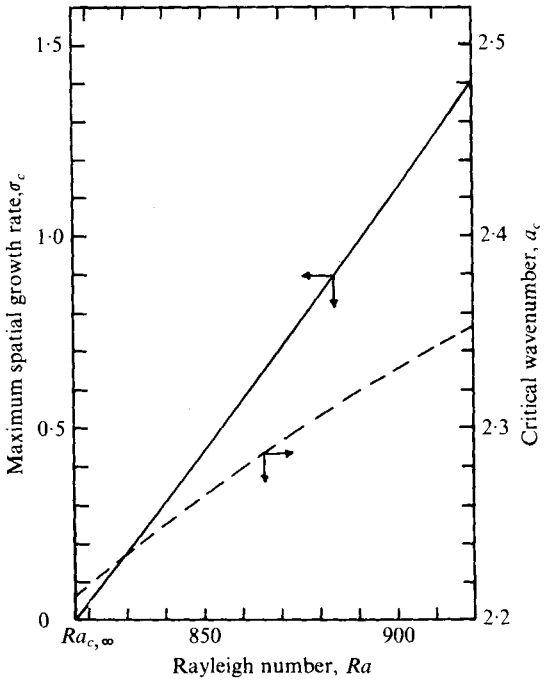


FIGURE 9. The maximum growth rate and critical wavenumber as a function of Rayleigh number in the asymptotic limit of a linear undisturbed temperature profile.

## 8. Local stability analysis for the thermal entry region

If it is assumed that the onset of thermal convection is controlled by the local temperature distribution just upstream of the onset, i.e. that the rate of change of the temperature profile in the axial direction can be neglected, (31) simplifies to the secular equation

$$|\mathbf{Q} + Ra\,\mathbf{R}(\xi)\,(\mathbf{H}-\mathbf{L})^{-1}\,\mathbf{M}| = 0. \tag{40}$$

The determination of $Ra_c$ and $a_c$ follows the procedure discussed above for the asymptotic analysis, but in this case $Ra_c$ is a function of $\xi$ because of the developing temperature profile. For any particular axial position a neutral-stability curve is generated and the minimum $Ra$ on that curve is considered to be the critical Rayleigh number above which thermal convection initiates at that position. Figure 10 shows a composite of such neutral-stability curves for various axial positions up to the asymptotic limit, which occurs at $\xi > 1{\cdot}0$.

The critical Rayleigh number is seen to decrease as $\xi$ increases, while $a_c$ varies only slightly with $\xi$. The relatively flat shape of the neutral-stability curves in the vicinity of $a_c$ suggests that a fairly wide range of disturbance frequencies will lead to thermal convection for $Ra$ only slightly above $Ra_c$. It is not surprising that $Ra_c$ decreases sharply as $\xi$ increases, for at small values of $\xi$ the thermal boundary layer is thin, and only within this boundary layer do density variations occur. These results can be compared with the experimental heat-transfer data of figure 4 by plotting $Ra$ *vs.* the axial position of the minimum $Nu$ for each set of heat-transfer data. The results of this analysis and experiment are shown in figure 11 together with the results of Hung & Davis (1974*a*), who used a Runge–Kutta method to solve the governing equations for a local stability analysis.

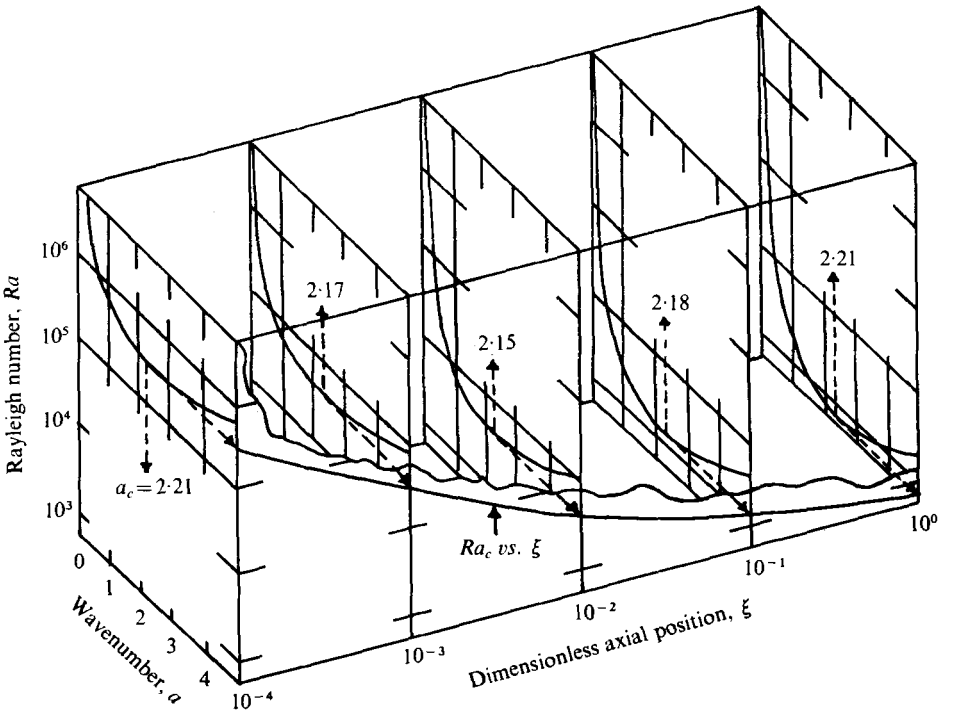


FIGURE 10. Neutral-stability curves for various axial positions based on local stability analysis.

It is clear from figure 11 that the local stability theory predicts Rayleigh numbers at the onset of thermal convection considerably lower than the experimental observations for small $\xi$, but the reason for this disagreement is not clear. The data for larger values of $\xi$ lie closer to the theoretical curve than those for small $\xi$, which suggests that the asymptotic results agree, but there are three possible explanations for the disagreement at small $\xi$.

(i) The disturbances detected experimentally do not correspond to the predictions of linear stability theory because the disturbances must grow sufficiently to be detected.

(ii) The neglect of the axial variation of the temperature profile is not valid.

(iii) The use of the film thickness $d$ as the scaling factor does not adequately take into account the fact that the thermal convection is largely confined to the thermal boundary layer.

We shall examine point (i) in some detail in the section on amplification theory. Points (ii) and (iii) will be examined simultaneously below, and it will be concluded that a modified local stability theory adequately describes the experimental data.

## 9. The modified local stability analysis

There is some experimental indication that at the onset of thermal convection the disturbances are confined to a thin region near the heated surface. Although the velocity disturbances are controlled mainly by the boundary conditions at the fixed and free surfaces, it seems reasonable to assume that the temperature disturbances are

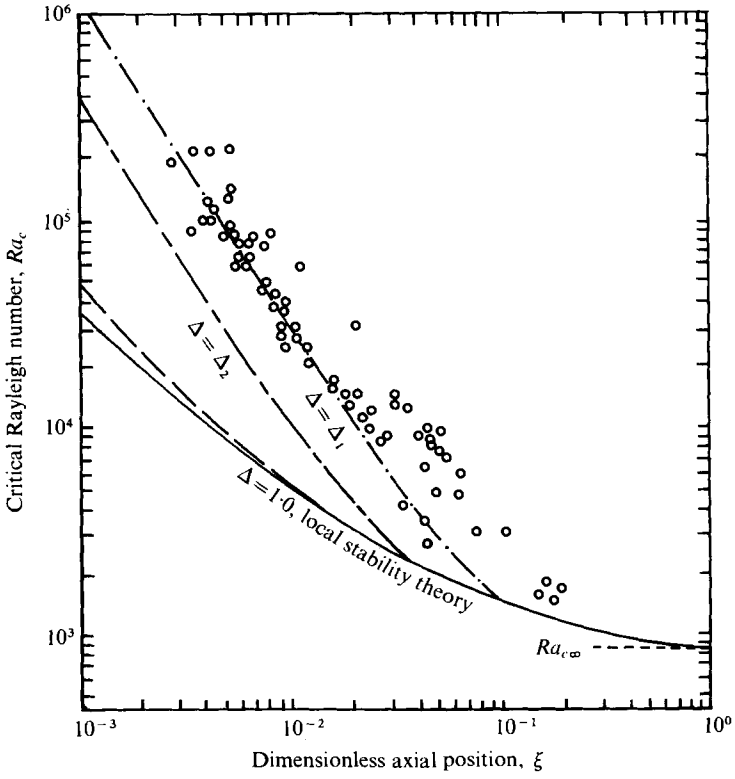


FIGURE 11. A comparison between theory and experiment for the onset of cellular convection. ○, water data; — —, Runge–Kutta method.

confined to the thermal boundary layer produced by the forced convection. We shall reformulate the problem using this premise to generate a modified local stability theory.

Equations (18) and (19) still apply and the hydrodynamic boundary conditions (20) remain the same, but the thermal boundary condition at $\zeta = 1$ will be replaced by

$$\hat{\theta}(\xi, \zeta) = 0 \quad \text{for} \quad \Delta \leqslant \zeta \leqslant 1,$$

where $\Delta$ is the non-dimensional thermal boundary-layer thickness derived from the undisturbed temperature field. There is some arbitrariness at this point, for we must define $\Delta$ quantitatively. It is conventional in boundary-layer theory to define $\Delta$ as the distance from the heated surface at which the temperature difference $T_w - T$ is 99% of $T_w - T_\infty$, where $T_w$ and $T_\infty$ are the wall temperature and bulk temperature, respectively. In our application $T_\infty$ can be taken to be the constant surface temperature. We shall use this definition for $\Delta$, and to examine the effects of various possible definitions of $\Delta$ we shall also use a 99·99% criterion. These two policies can be used together with the Leveque solution for the unperturbed temperature to give

$$\Delta_1 = (10{\cdot}4\xi)^{\frac{1}{3}} \quad \text{for} \quad \xi \leqslant 0{\cdot}096, \tag{41}$$

$$\Delta_2 = (28\xi)^{\frac{1}{3}} \quad \text{for} \quad \xi \leqslant 0{\cdot}036. \tag{42}$$

The previous analysis is equivalent to $\Delta = 1$.

Now, using trial functions only slightly modified from (22) and (25), the resulting governing equations are solved by the method discussed in the previous sections to

obtain the additional curves marking the onset of natural convection shown in figure 11. The prediction based on $\Delta_1$ is in surprisingly good agreement with experiments over the whole range of Rayleigh numbers studied. Both the slope of the theoretical curve of $Ra_c$ *vs.* $\xi_c$ and the absolute values are consistent with the experimental data, whereas both the slope and the values predicted by the original local stability analysis disagree with the experiments.

Although some data points lie below the theoretical prediction, it should be pointed out that our calculations were for large $Pr$ while the experiments were performed with water, for which $Pr \sim 7$. As shown by Hung & Davis (1974*a*), the effect of a lower $Pr$ on the analysis is to lower the predicted values of $Ra_c$ somewhat. One would normally expect most of the data points to lie above the predictions from linear stability theory because of the finite distance required for instabilities to grow to a discernible size as mentioned above.

The results of the modified local stability analysis for the onset of cellular convection suggest that the instability develops within the thermal boundary layer and that the concept of local stability, which neglects the axial rates of change of the temperature profile, has some validity. But there remains one additional set of information to be examined: the wavenumber of the roll cells.

## 10. Wavenumbers

Figure 10 indicates that the critical wavenumbers corresponding to the onset of the cellular mode of instability are predicted to be nearly constant over a wide range of $Ra_c$ by the original local stability theory. Numerous photographs were taken of the flow-visualization experiments to determine the widths of the roll cells (see figure 7, plate 2). The photographs show that the roll cells broaden somewhat with increasing axial distance and that some pinching of the roll cells occurs at larger distances, causing disturbances to the roll cells. However, near the onset of roll-cell formation usually 20 or more roll-cell boundaries could be distinguished across the tunnel bottom and an average roll-cell width could be measured from the photographs. Results of those measurements are plotted in figure 12 as $a_c$ *vs.* $Ra_c$. Also plotted on the figure are the predictions obtained using the local stability analyses. The local stability analysis with the film thickness as the length scale completely fails to predict the proper dependence of $a_c$ on $Ra_c$, while the modified local stability analysis predicts wavenumbers that are in reasonable agreement with the observed values but increase with $Ra_c$ at a smaller rate.

A factor possibly contributing to the difference between theory and experiment is that the analysis was limited to infinitely large Prandtl number, while the data are for $Pr \sim 7$. Although the Prandtl number has some effect on the critical wavenumber, as shown by Hung (1973), the differences are not likely to be due to this effect. Recent data taken in this laboratory for a glycerol–water solution ($Pr \sim 200$) show wavenumbers close to those for water.

## 11. Amplification theory

In the local stability analysis performed above we neglected the derivative $d\mathrm{C}/d\xi$ in (31) and solved the resulting secular equation to obtain the stability criterion for cellular convection. If we cease to neglect the axial rate of change of the temperature

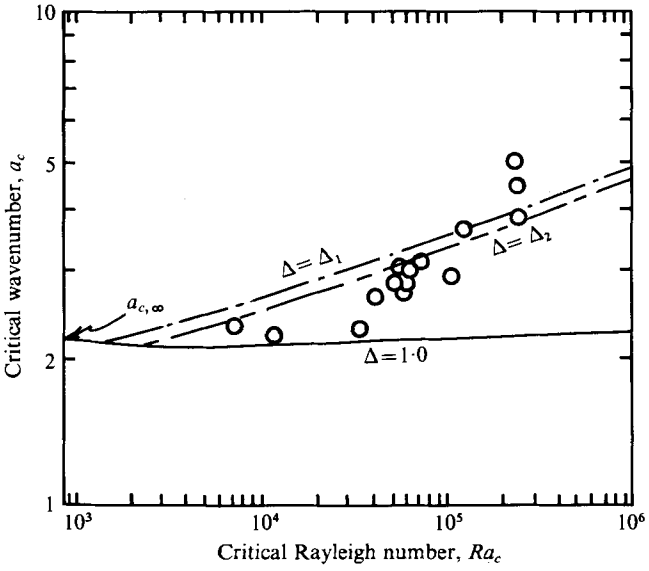


FIGURE 12. A comparison between theory and experiment for the wavenumbers of the cellular convection. ○, water data.

profile, we require inlet conditions to solve (31). This is a major difficulty associated with amplification theory, for in most experiments we have no control over and no knowledge of the inlet disturbances. One conventional approach is to consider the inlet disturbance to be 'white noise', i.e. to assume that disturbances of all wavenumbers exist and have the same amplitude. Moreover, we shall arbitrarily choose either $A_i(0) = 1$ or $C_j(0) = 1$ to define the inlet disturbance. In his analysis of the stability of a deep liquid pool cooled from above, Foster (1965) examined the effects of various initial conditions including 'white noise' with all the Fourier coefficients equal, finding that the latter policy led to the fastest growth rates. Mahler *et al.* (1968) concurred with Foster on this point, but Gresho & Sani (1971) pointed out that this policy of choosing the Fourier coefficients to be equal can lead to the prediction of unreasonable temperature perturbations. We shall examine this point in some detail below.

Since the solution of (31) subject to the prescribed inlet condition is obtained to within a multiplicative constant, we shall apply the usual criterion for measuring the magnitude of the perturbations: the amplification ratio

$$\overline{w}(\xi) = [\langle \hat{w}^2(\xi, \zeta)\rangle / \langle \hat{w}^2(0, \zeta)\rangle]^{\frac{1}{2}}. \tag{43}$$

This amplification ratio is the one used by Foster (1965) and all subsequent investigators and is appropriate when it is the velocity perturbations that are observed and used as the criterion for the onset of the instability. In the experiments associated with this work both flow visualization and heat-transfer measurements were used to identify the onset of discernible perturbations. To interpret the heat-transfer measurements it is more appropriate to define a Nusselt number amplification ratio $\overline{Nu}$ as

$$\overline{Nu}(\xi) = \left| \frac{\hat{\theta}(\xi, 0) - \hat{\theta}_b(\xi)}{\hat{\theta}(0, 0) - \hat{\theta}_b(0)} \right|, \tag{44}$$

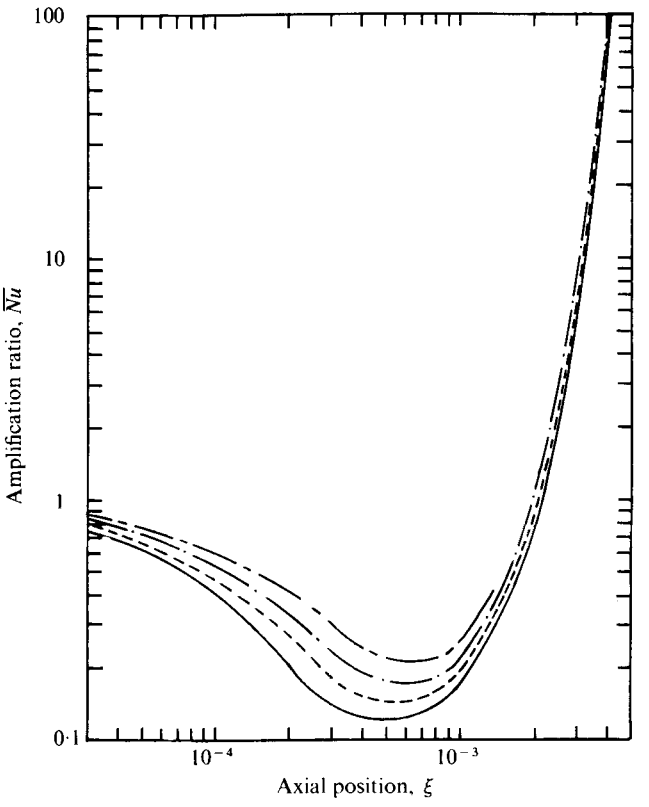


FIGURE 13. The effect of the number of simultaneous equations used on the thermal amplification ratio $\overline{Nu}$. $Ra = 5 \times 10^4$, $a = 3{\cdot}6$, ——, $N = 15$, – – –, $N = 14$; —·—, $N = 13$; — – —, $N = 12$.

where the amplitude perturbation of the bulk temperature $\hat{\theta}_b(\xi)$ is given by

$$\hat{\theta}_b(\xi) = \int_0^1 2\zeta\hat{\theta}(\xi, \zeta)\, d\zeta. \tag{45}$$

Figure 4 indicates how the heat-transfer measurements were used to define the onset of discernible buoyancy-driven convection. In the upstream region of the heated section the Nusselt numbers follow the predictions of the Graetz solution for pure forced convection. At an axial position that depends on the Rayleigh number the measured Nusselt number passes through a minimum and begins to deviate from the Graetz solution. We define the axial position of this minimum to be the point $\xi_c$ at which the convective perturbations are large enough to be discernible. We shall apply both $\overline{w}(\xi)$ and $\overline{Nu}(\xi)$ to interpret experimental results.

To solve the system of equations summarized by (31) we used the fourth-order Runge–Kutta–Gill method. The step size was selected such that the single-step error was less than 0·1 % in a predictor–corrector integration method. For the results presented below we truncated the system to 15 equations after examining the effect of the number of equations $N$ on the calculated amplification ratios. Typical results showing the effect of $N$ on the calculated amplification ratio $\overline{Nu}$ are presented in figure 13.

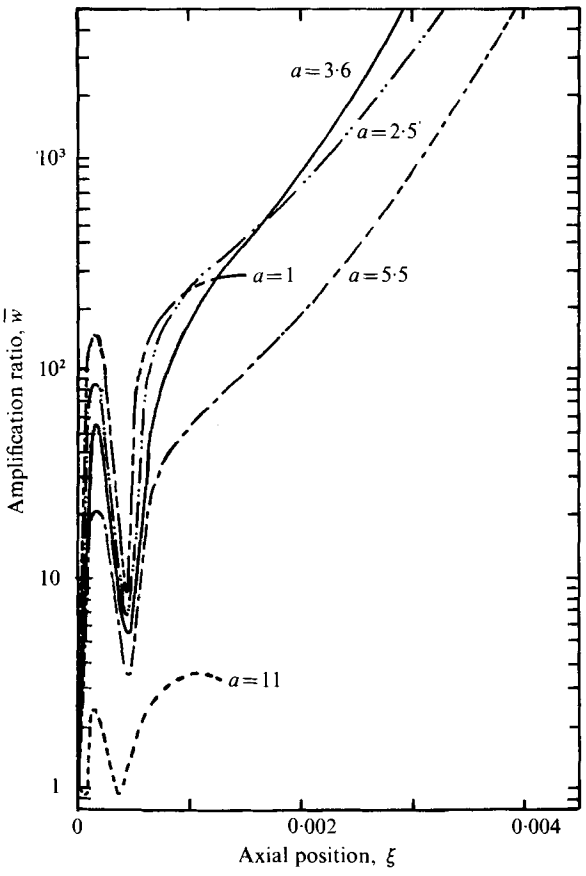


FIGURE 14. The effect of wavenumber on the velocity amplification ratio $\overline{w}$ for a 'white noise' velocity disturbance inlet condition (WNV). $Ra = 5 \times 10^4$, $N = 12$.

## 12. Results of amplification theory

Equation (31) involves the parameters $a$ and $Ra$, so numerical calculations were carried out for several values of $Ra$ with $a$ varied to obtain the wavenumber with the largest growth rate. Typical results are shown in figure 14 as $\overline{w}$ *vs.* $\xi$ using a 'white noise' velocity disturbance as the inlet condition. For this case ($Ra = 5 \times 10^4$) the largest growth rate was found for $a = 3{\cdot}6$. The wavenumber $a_{\max}$ of the disturbance with the largest growth rate is not sharply defined, and figure 14 shows that the slopes of the curves for $a = 3{\cdot}6$ and $a = 5{\cdot}5$ are not greatly different for sufficiently large $\xi$. We shall discuss this behaviour in more detail below.

The effect of $Ra$ on $a_{\max}$ and on the amplification ratio $\overline{w}$ is shown in figure 15. The cusps that occur for $Ra \leqslant 3{\cdot}5 \times 10^5$ do not seem to be physically realistic and are probably the result of the rather artificial and arbitrary inlet value of $\hat{w}(0, \zeta)$ imposed. For $Ra > 3{\cdot}5 \times 10^5$ the curves increase monotonically. Also shown in figure 15 is the solution corresponding to $Ra_{c,\infty}$ and $a_{c,\infty}$, the critical conditions obtained for the asymptotic limit using marginal-stability concepts. The curve can be expected to reach a constant asymptotic value beyond $\xi = 0{\cdot}1$ since no growth or decay of disturbances should occur for these critical conditions in the asymptotic limit of large $\xi$.

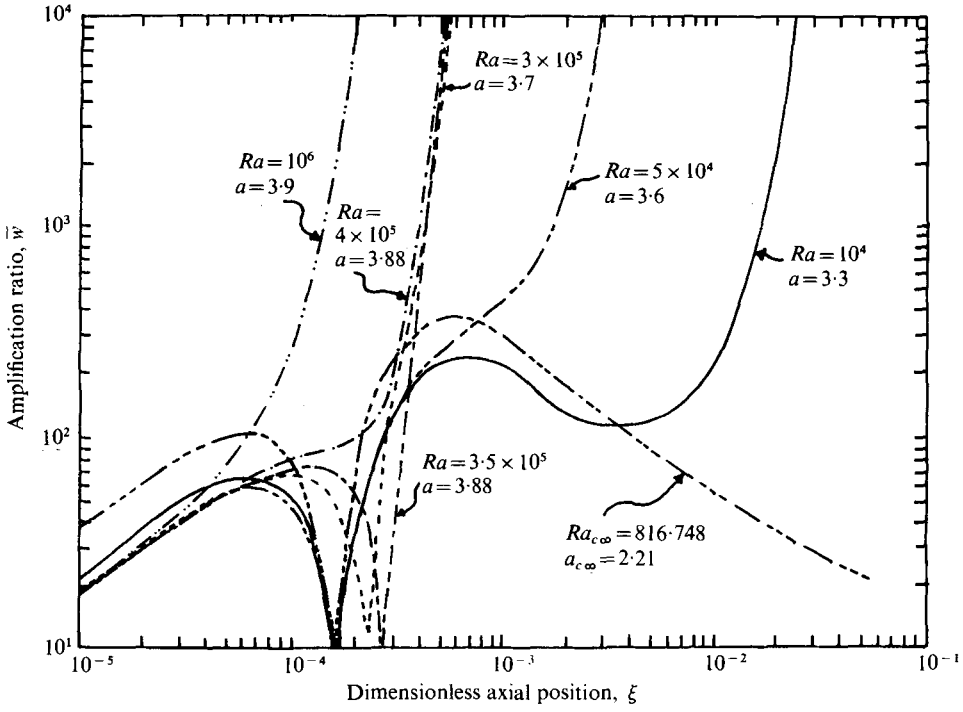


FIGURE 15. The effects of Rayleigh number on the wavenumber $a_{max}$ of the fastest-growing disturbance and on the amplification ratio $\bar{w}$.

The effect of the inlet conditions on the solution has been considered by using a 'white noise' inlet temperature disturbance (to be referred to as WNT) rather than the 'white noise' velocity disturbance (WNV), i.e. by choosing $C_j(0) = 1$ in (25) rather than $A_i(0) = 1$ in (22). For $Ra = 5 \times 10^4$ we obtained $a_{max} = 3{\cdot}87$, which is not significantly different from the result obtained using WNV. The solution for $\bar{w}$ is, however, significantly different as shown in figure 16 for three different values of $Ra$. The solutions obtained using WNT do not show the cusp encountered using WNV, which suggests further that the cusps are a result of an incompatibility between the inlet condition and the behaviour of the governing equations.

A similar conclusion can be drawn by examining $\overline{Nu}(\xi)$ rather than $\bar{w}(\xi)$. For WNT the solution is well behaved as seen in figure 17, but for WNV cusps occur at the lower Rayleigh numbers. The values of $a_{max}$ obtained for WNT are generally slightly larger than for WNV, but the differences are not very significant considering the fact that the growth rates are not very sensitive to $a$ in the vicinity of $a_{max}$.

A convenient method of indicating the effect of $Ra$ on $\hat{w}$ and $\hat{\theta}$ is to examine the normalized functions $w^* = \hat{w}(\xi, \zeta)/\hat{w}_{max}(\xi)$ and $\theta^* = \hat{\theta}(\xi, \zeta)/\hat{\theta}_{max}(\xi)$ at axial positions where the amplification ratio $\overline{Nu}$ has some specified value. Here $\hat{w}_{max}$ and $\hat{\theta}_{max}$ are the maxima of the functions $\hat{w}$ and $\hat{\theta}$ respectively, considered as functions of vertical position $\zeta$. Figure 18 shows $w^*$ and $\theta^*$ for various values of $Ra$ evaluated where $\overline{Nu} = 10^3$. The normalized disturbance velocity amplitude $w^*$ is nearly independent of $Ra$, and is nearly parabolic. The normalized disturbance temperature amplitude $\theta^*$ shows a distinctive boundary-layer character with the boundary-layer thickness

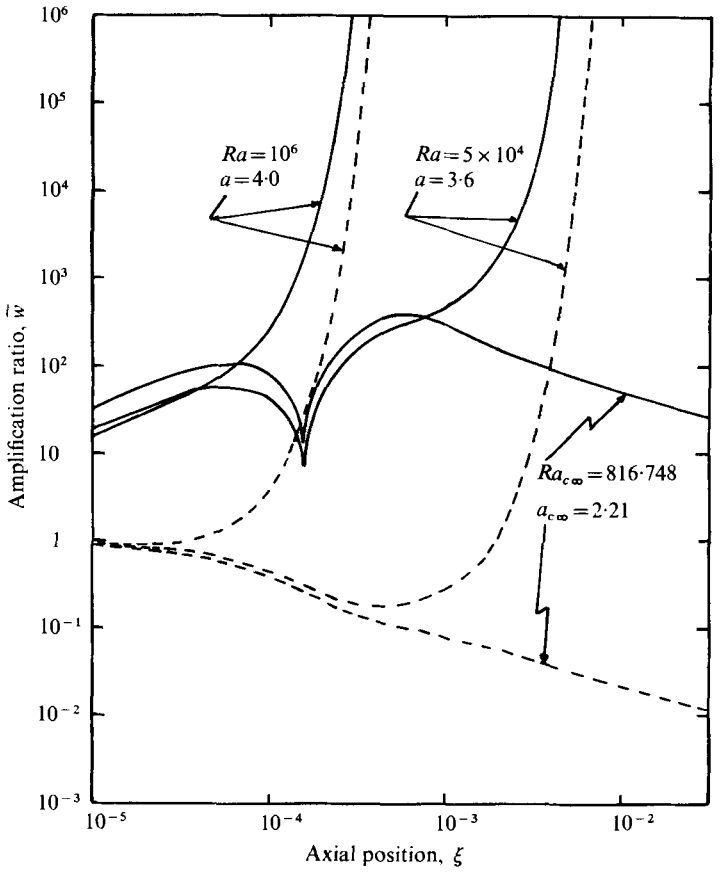


FIGURE 16. The velocity amplification ratio $\bar{w}$ for 'white noise' temperature (WNT) and velocity (WNV) disturbance inlet conditions. ——, WNV; – – –, WNT.

decreasing with increasing $Ra$ at the axial positions where $\overline{Nu} = 10^3$. We should point out that this axial position is much greater for smaller $Ra$ than for large $Ra$ because an amplification of $10^3$ will require greater distances as $Ra$ decreases. Thus, from figure 18 we conclude that the primary effect of $Ra$ on $\hat{w}$ is to alter its magnitude but not its functional dependence on $\xi$.

## 13. Comparison with experiments

The results shown in figures 15 and 16 can be compared with experimental data on the onset of discernible natural convection by plotting the loci of points $Ra$ *vs.* $\xi$ corresponding to fixed values of the amplification ratios $\bar{w}$ and $\overline{Nu}$. Figure 19 is a comparison of such loci with our experimental data. Also plotted on the figure are the results of marginal-stability analysis using the 'frozen' or quasi-steady model for the undisturbed temperature profile. The experimental points are based on the heat-transfer measurements discussed above.

The curves for $\overline{Nu} = 10^3$ and $10^4$ are very nearly parallel to, but lie above, the curve based on the quasi-steady model. The axial distance between these solutions is the distance required for infinitesimal disturbances to amplify by the specified amount.

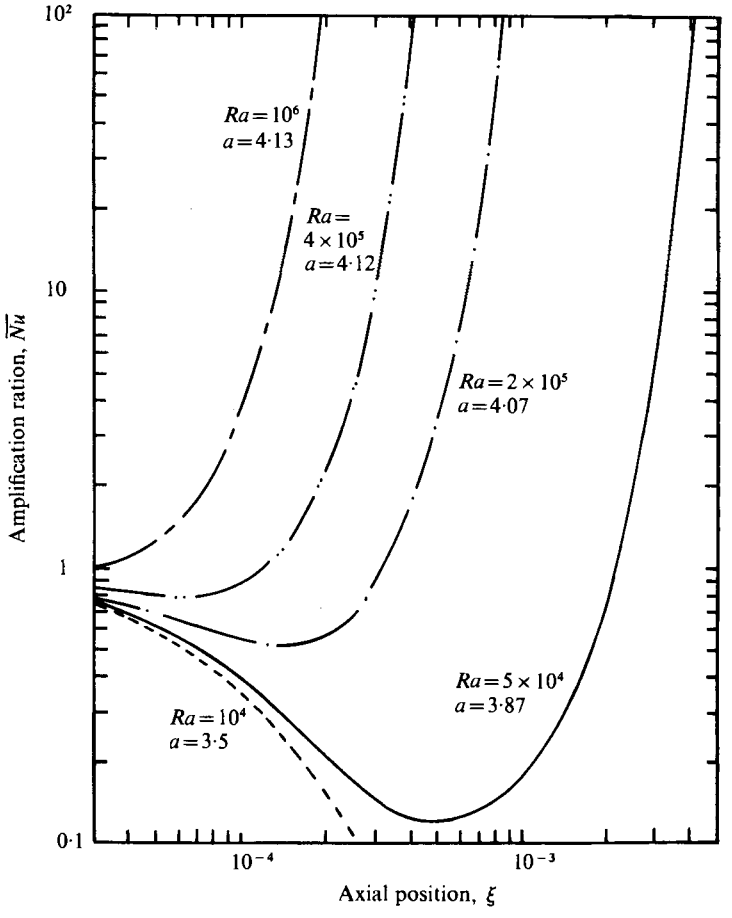


FIGURE 17. The thermal amplification ratio $\overline{Nu}$ for a 'white noise' temperature disturbance inlet condition (WNT).

The curves for $\overline{w} = 10^3$, $10^4$ and $10^6$ show more upward curvature at larger $Ra$ than the curves of constant $\overline{Nu}$, but for lower $Ra$ the curves have essentially the same slopes.

It is clear from figure 19 that the onset of measurable cellular convection indicated by the experimental points does not correspond to any single amplification ratio. For $Ra = O(10^4)$ the data are consistent with $\overline{Nu} = 10^3$, but at higher $Ra$ larger amplification ratios must be postulated to explain the data. These results are similar to those of Davenport & King (1974*a*) for the temporal growth of disturbances in initially quiescent liquid pools. Their data for organic liquids are consistent with amplification ratios in the range $10^1 < \overline{w} < 10^4$ for Rayleigh numbers in the range $300 < Ra < 3000$ and Prandtl numbers in the range $7 < Pr < 10^4$.

It must be pointed out that $Pr \simeq 7$ in our experiments while we have limited our analysis to the asymptotic limit of large $Pr$. Foster (1965), Mahler *et al.* (1968) and Gresho & Sani (1971) have all examined the effect of Prandtl number on the growth rates for the time-dependent problem. Their results indicate that for a particular $Ra$ the time required to reach a specified amplification ratio $\overline{w}$ increases with decreasing Prandtl number for $1 < Pr < 100$. For $Pr > 100$ the results for infinite Prandtl

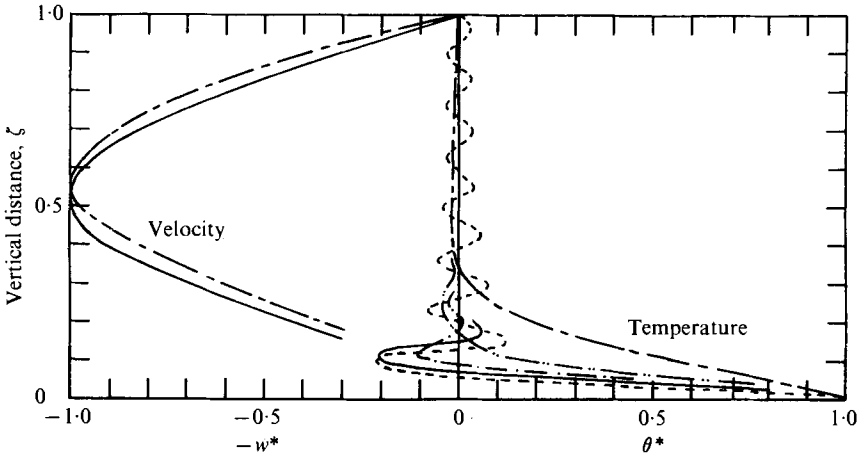


FIGURE 18. The normalized amplitude functions $w^*$ and $\theta^*$ for various Rayleigh numbers. – – –, inlet disturbance; — – —, $Ra = 10^4$, $a = 3{\cdot}50$; —. .—, $Ra = 5 \times 10^4$, $a = 3{\cdot}87$; —·—, $Ra = 20 \times 10^4$, $a = 4{\cdot}06$; ——, $Ra = 100 \times 10^4$, $a = 4{\cdot}13$.

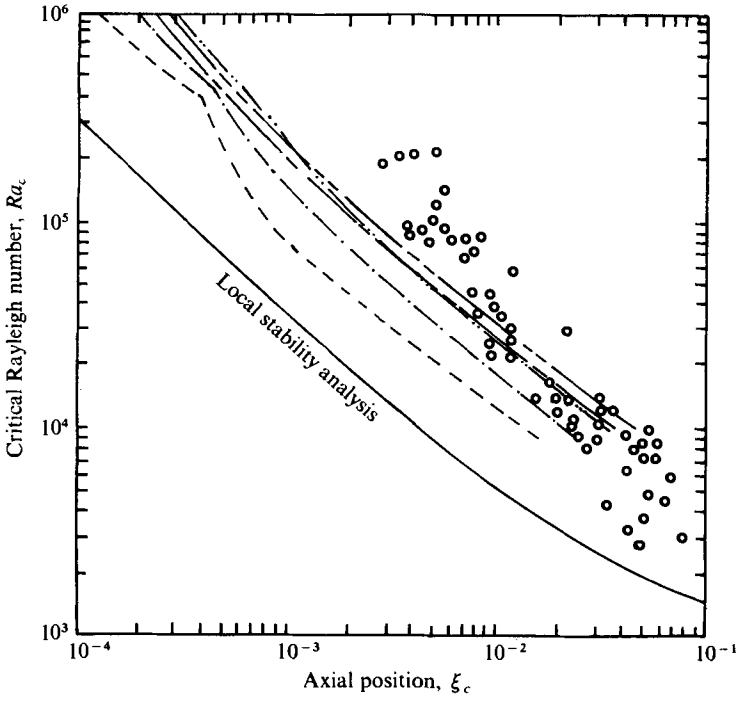


FIGURE 19. Comparison of the axial positions of the measured onset of discernible thermal disturbances with the predictions of amplification theory. ○, water data; — – – —, WNT, $\overline{Nu} = 10^4$; — – —, WNT, $\overline{Nu} = 10^5$; —··—, WNV, $\overline{w} = 10^6$; —·—, WNV, $\overline{w} = 10^4$; – – –, WNV, $\overline{w} = 10^3$.

number apply. The calculations of Foster (1965) for $Ra = 10^6$ and Gresho & Sani (1971) for $Ra = 10^5$ show that the critical time required to attain a specific amplitude ratio with $Pr = 7$ is increased by 40–70% over the critical time with $Pr > 100$.

By analogy, then, we can expect the distance required to reach a specified value of either $\overline{Nu}$ or $\overline{w}$ to be somewhat greater for $Pr = 7$ than for infinitely large $Pr$. The

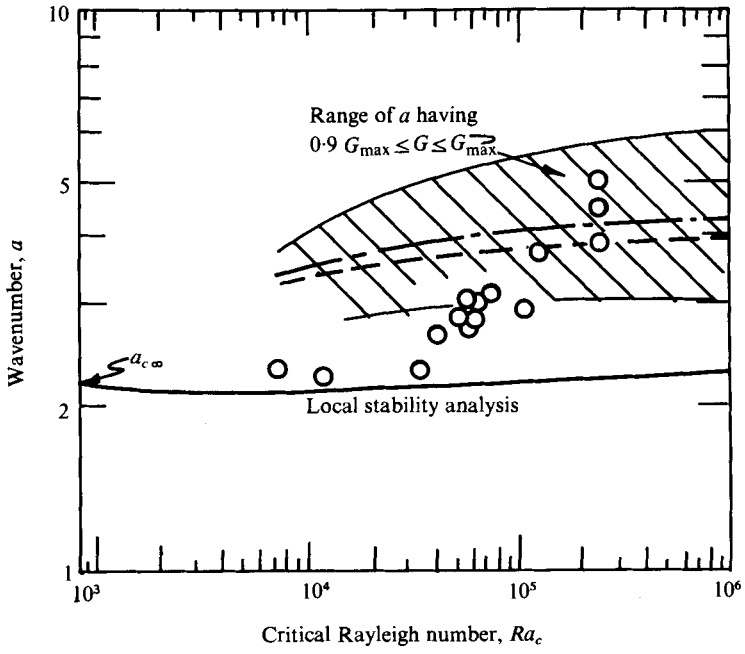


FIGURE 20. Comparison of measured average wavenumbers with the predictions from amplification theory. ○, water data, — — —, theory for WNT; – – –, theory for WNV.

effect on the solutions shown in figure 19 would be to shift the curves for constant $\overline{Nu}$ and $\overline{w}$ to the right, but a factor of two would be insufficient to affect our conclusions. Recent data for a glycerol–water solution with $Pr = 200$ do not show a significant Prandtl number effect on the position of the onset of cellular convection.

Because experimental observations do not conform to any single amplification ratio over a range of Rayleigh numbers, the utility of amplification theory for predicting the onset of cellular convection is questionable, but it is clearly an improvement over quasi-steady marginal-stability analysis. Although the results of amplification theory lack uniqueness (in the sense that a definitive statement about the onset of discernible disturbances cannot be made without recourse to experiments), we can evaluate amplification theory by examining predicted and experimental wavenumbers. From our flow-visualization experiments, such as that shown in figure 7, we observe that the roll cells formed are not perfectly uniform in width across the heated surface even if we neglect the effects of the side walls on the first few roll cells near the walls. But we can obtain a meaningful average wavenumber by measuring the dimensions of twenty or thirty roll cells in the central portion of the test section for runs at various Rayleigh numbers. Figure 20 shows such experimental wavenumbers as a function of Rayleigh number and also the theoretical results for $a_{max}$ obtained from amplification theory. Since the wavenumbers of the fastest-growing disturbances differed slightly for the 'white noise' inlet temperature disturbance and the 'white noise' inlet velocity disturbance, we have plotted both results, indicated by WNT and WNV respectively.

The experimental wavenumbers are generally lower than the theoretical values and increase with $Ra$ at a greater rate than theory suggests. A possible explanation can be found by examining the effect of the wavenumber on the growth rate in the

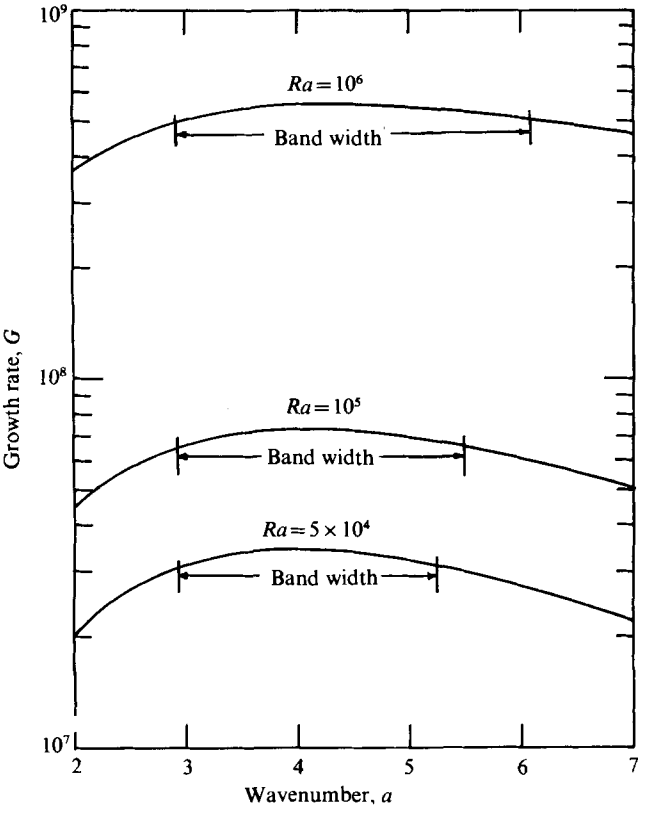


FIGURE 21. The growth rate $G$ for various wavenumbers and Rayleigh numbers in the vicinity of the fastest-growing wavenumber. $\overline{Nu} = 10^4$ for WNT.

vicinity of $a_{\max}$. For purposes of comparison let us define the growth rate of temperature disturbances by $G = d\overline{Nu}/d\xi$. Figure 19 indicates that disturbances that have amplified by $\overline{Nu} = 10^4$ are discernible, so we shall examine growth rates for $\overline{Nu} = 10^4$ as a function of wavenumber and Rayleigh number. Figure 21 is a plot of $G$ *vs.* $a$ and shows that the growth rate is not very sensitive to the disturbance wavenumber in the neighbourhood of $a_{\max}$, especially at larger Rayleigh numbers. Thus it is difficult to establish $a_{\max}$ with high precision. Furthermore, these results suggest that at any particular Rayleigh number there is a band of wavenumbers that have growth rates near the maximum growth rate, and the width of the band increases with increasing Rayleigh number. Spangenberg & Rowland (1961) and Berg, Boudart & Acrivos (1966) have suggested that this characteristic of amplification theory explains why chaotic motion rather than a well-defined cell structure is frequently observed in Bénard's (1900) experiment.

In the present problem of a flowing liquid film the cellular convection is fairly regular, but variations in both roll-cell width and the position of the onset of discernible disturbances are observed and suggest that a sharply defined wavenumber does not occur experimentally. To show that wave amplitude theory can be used to explain the variations we have plotted on figure 21 the range of wavenumbers having growth rates within 10% of the maximum growth rate. There is a distinct shift towards

higher wavenumbers when we consider such bands. Thus if a range of wavenumbers is observed experimentally there is a tendency for the average to be greater than $a_{max}$. This tendency together with the effect of Prandtl number on $a_{max}$ can explain the differences between theory and experiment shown in figure 20.

## 14. Conclusions

The onset of cellular convection in a flowing liquid layer has been analysed by applying local stability analysis and amplification theory for the spatial growth of disturbances. The local (marginal) stability analysis using the liquid depth as the length scaling factor greatly underpredicts the critical Rayleigh number for the onset of cellular convection, and it predicts critical wavenumbers that are nearly independent of the Rayleigh number.

Thermal amplification ratios $\overline{Nu}$ of order $10^3$ and larger are required to obtain agreement with experimental data on the dependence on the Rayleigh number of the critical axial position for discernible cellular convection. Velocity amplification ratios $\overline{w}$ larger than $10^4$ must be postulated to explain the data. The experimental data are in considerably better agreement with a modified marginal-stability analysis than with amplification theory. Classical marginal-stability analysis fails to predict satisfactorily either the position of the onset of discernible cellular convection or the dependence of the wavenumber on the Rayleigh number.

The two analyses, amplification theory and the modified stability analysis, predict wavenumbers (for $Pr \to \infty$) in fair agreement with those observed experimentally (for $Pr \sim 7$), and amplification theory predicts a flattening of the wavenumber *vs.* Rayleigh number curve at high Rayleigh numbers that is not seen experimentally. The modified marginal-stability analysis, which assumes that cellular convection is confined to the thermal boundary layer, predicts that $a_{max}$ increases with Rayleigh number at a greater rate than does amplification theory, and the best agreement with experiment is obtained by means of the modified local stability analysis.

All of the theoretical approaches predict a flattening of the growth rate *vs.* wavenumber curve as the Rayleigh number increases, i.e. that the growth rate becomes less sensitive to wavenumber as the Rayleigh number increases. Hence, if a band of wavenumbers have growth rates not differing greatly from the maximum growth rate, of the wavenumber $a_{max}$, it is likely that all of these will become discernible at approximately the same axial position. The experiments confirm this speculation, for flow-visualization experiments show a rather jagged onset of observable roll cells and variations in the roll-cell width.

It should be pointed out that the cellular convection analysed here undergoes a second instability at $Ra > 10^5$. Our experiments (see figure 7) show that transverse motion of the roll cells begins at higher Rayleigh numbers, and the flow becomes turbulent. Although we have made numerous observations of the second instability, we have not studied the phenomenon systematically to determine its characteristics and effects on heat transfer.

This work was supported by National Science Foundation Grant GK 41270 and the Design Institute for Multiphase Processing (DIMP) of the American Institute of Chemical Engineers.

## REFERENCES


BÉNARD, H. 1900 *Rev. Gén. Sci. Pures Appl.* **11**, 1261.

BERG, J. C., ACRIVOS, A. & BOUDART, M. 1966 *Adv. in Chem. Engng* **6**, 61.

BERG, J. C., BOUDART, M. & ACRIVOS, A. 1966 *J. Fluid Mech.* **24**, 721.

BLAIR, L. M. & QUINN, J. A. 1969 *J. Fluid Mech.* **36**, 385.

CHANDRASEKHAR, S. 1961 *Hydrodynamic and Hydromagnetic Stability*. Oxford: Clarendon Press.

CHOI, C. K. 1976 Ph.D. thesis, Clarkson College of Technology.

CURRIE, I. G. 1967 *J. Fluid Mech.* **20**, 337.

DAVENPORT, I. F. & KING, C. J. 1974*a* *Int. J. Heat Mass Transfer* **17**, 69.

DAVENPORT, I. F. & KING, C. J. 1974*b* *Int. J. Heat Mass Transfer* **17**, 77.

DAVIS, E. J. 1973 *Can. J. Chem. Engng* **51**, 562.

FOSTER, T. D. 1965 *Phys. Fluids* **8**, 1249.

FOSTER, T. D. 1968 *Phys. Fluids* **11**, 1257.

FRISK, D. P. & DAVIS, E. J. 1972 *Int. J. Heat Mass Transfer* **15**, 1537.

GRESHO, P. M. & SANI, R. L. 1971 *Int. J. Heat Mass Transfer* **14**, 207.

GUMERMAN, R. J. & HOMSY, G. M. 1974*a* *A.I.Ch.E. J.* **20**, 981.

GUMERMAN, R. J. & HOMSY, G. M. 1974*b* *A.I.Ch.E. J.* **20**, 1161.

HUNG, S. C. 1973 Ph.D. thesis, Clarkson College of Technology.

HUNG, S. C. & DAVIS, E. J. 1974*a* *A.I.Ch.E. J.* **20**, 194.

HUNG, S. C. & DAVIS, E. J. 1974*b* *Int. J. Heat Mass Transfer* **17**, 1357.

LICK, W. 1965 *J. Fluid Mech.* **21**, 565.

MAHLER, E. G., SCHECHTER, R. S. & WISSLER, E. H. 1968 *Phys. Fluids* **11**, 1901.

MORTON, B. R. 1957 *Quart. J. Mech. Appl. Math.* **10**, 433.

NIELSEN, R. C. & SABERSKY, R. H. 1973 *Int. J. Heat Mass Transfer* **16**, 2407.

PLEVAN, R. E. & QUINN, J. A. 1966 *A.I.Ch.E. J.* **12**, 894.

RAYLEIGH, LORD 1916 *Phil. Mag.* **32**, 529.

SOBERMAN, R. K. 1959 *Phys. Fluids* **2**, 131.

SPANGENBERG, W. G. & ROWLAND, W. R. 1961 *Phys. Fluids* **4**, 743.

SPARROW, F. M., GOLDSTEIN, R. J. & JONSSON, V. K. 1964 *J. Fluid Mech.* **18**, 513.

TOBIAS, C. W. & HICKMAN, R. G. 1965 *Z. Phys. Chem.* **229**, 145.

WHITEHEAD, J. A. 1971 *Am. Scientist* **59**, 444.

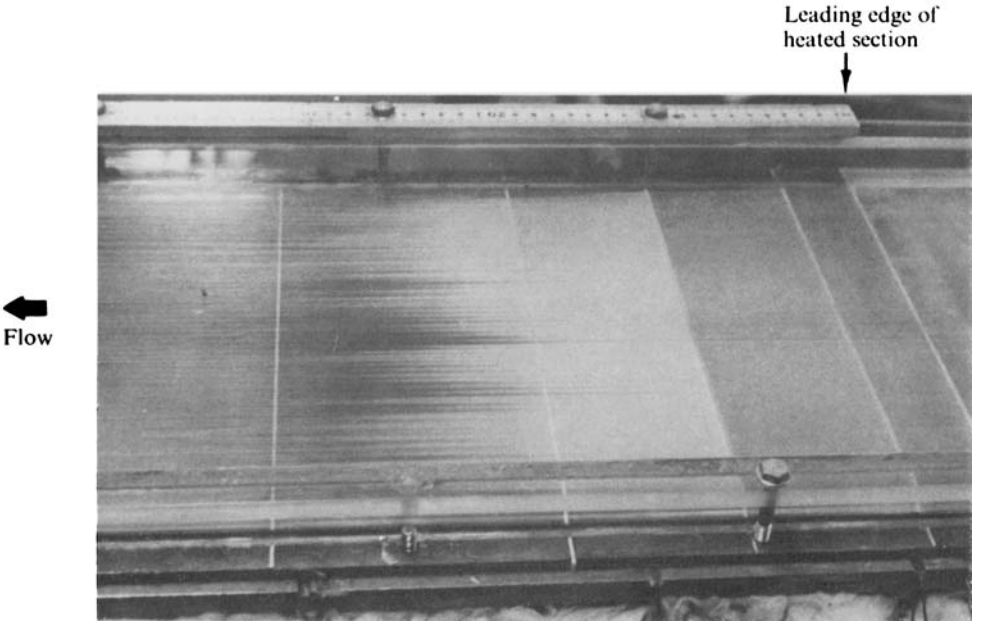


FIGURE 5. A view of the heat-transfer section showing deposition of colloidal particles caused by longitudinal roll cells.

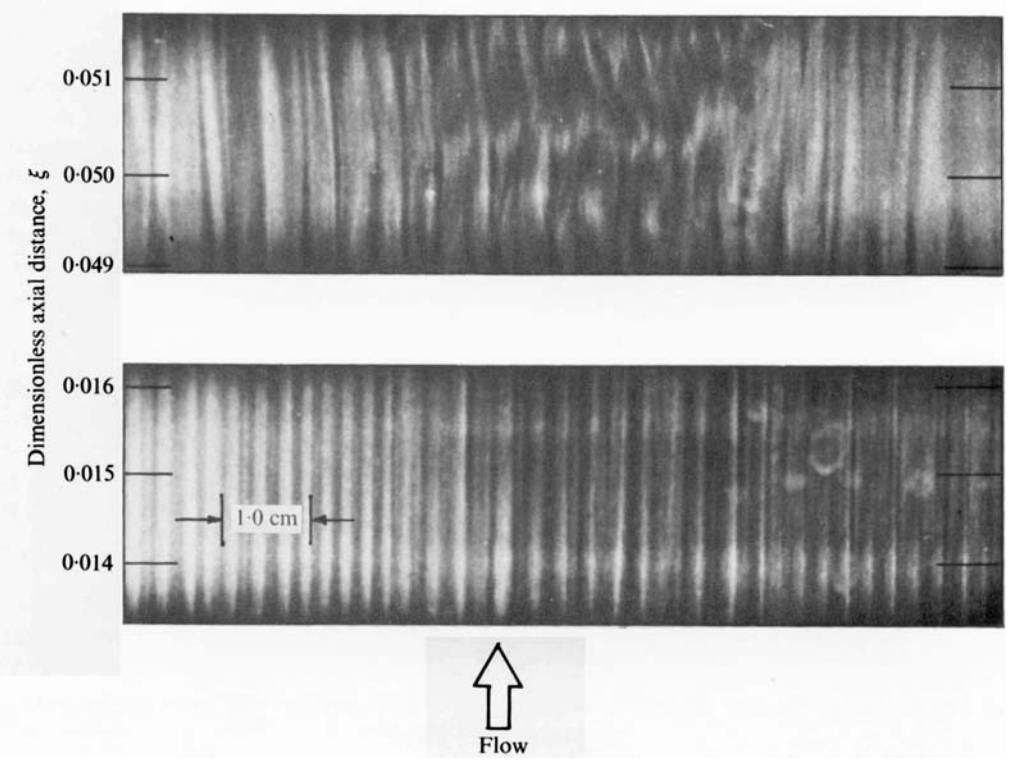


FIGURE 7. Flow visualization of the longitudinal roll cells in the upstream and downstream portions of the heat-transfer test section.